AGU ADVANCING EARTH AND SPACE SCIENCES

Space Weather

RESEARCH ARTICLE
10.1029/2023SW003714

Key Points:
- The observed difference of Slant total electron content (TEC) (difference of slant total electron content (dSTEC)) series is biased when an equatorial plasma bubble (EPB) occurred at the highest satellite elevation
- The error of GIM-TEC can increases (76%) or decreases (24%) during EPB event and its variation sign is unrelated to the magnitude of EPB
- The structure of EPB is unable to be captured by the GIM-TEC due to the low spatial-temporal resolution and linear interpolation method

Correspondence to:
W. Chen,
wu.chen@polyu.edu.hk

Citation:
Tang, L., Zhang, F., & Chen, W. (2024). The error of global ionospheric map-TEC during equatorial plasma bubble event in the high solar activity year. *Space Weather*, *22*, e2023SW003714. https://doi.org/10.1029/2023SW003714

Received 11 SEP 2023
Accepted 16 MAY 2024

The Error of Global Ionospheric Map-TEC During Equatorial Plasma Bubble Event in the High Solar Activity Year

Long Tang[1,2], Fenkai Zhang[1], and Wu Chen[2]

[1]School of Civil and Transportation Engineering, Guangdong University of Technology, Guangzhou, China, [2]Department of Land Surveying and Geo-Informatics, Hong Kong Polytechnic University, Hong Kong, China

Abstract In this study, the error of total electron content (TEC) derived from the global ionospheric map (GIM) (GIM-TEC) during equatorial plasma bubble (EPB) event is investigated for the first time. The frequently-used assessment parameter of ionospheric TEC model, namely difference of Slant TEC (difference of slant total electron content (dSTEC)) is checked and employed based on eight global navigation satellite system (GNSS) stations distributed around the geomagnetic equator during the high solar activity year of 2014. The international GNSS service final GIM products are exemplified. The results present several interesting findings: (a) The observed dSTEC series is biased when an EPB is observed at the highest satellite elevation, leading to a fake bias in GIM-TEC; (b) When an EPB occurred, the error of GIM-TEC can increases or decreases and its variation sign is unrelated to the magnitude of EPB; (c) The average of the EPB-induced GIM-TEC errors is mainly at −5 to 5 TECU with 76% (24%) of positive (negative) values, and the maximum (minimum) is close to 10 TECU (−10 TECU); (d) The structure of EPB is unable to be captured by the GIM-TEC series.

Plain Language Summary The global ionospheric map (GIM) derived total electron content (TEC) (GIM-TEC) is one kind of frequently-used data in ionospheric monitoring, GNSS positioning and other related areas. So, investigating the error of GIM-TEC is an important work before using it. The performance of GIM products is closely related to ionospheric variations. One kind of space weather event, namely geomagnetic disturbance, is usually discussed in pervious literature. In this study, we investigate another kind of common ionospheric variation called equatorial plasma bubble (EPB). The EPB is generally occurred after sunset and can cause ionospheric TEC depletion, thereby generating huge TEC gradients. The results show the most errors of GIM-TEC are increased during EPB event. In addition, the structure of EPB is unable to be captured by the GIM-TEC series due to the low spatial-temporal resolution and linear interpolation method.

1. Introduction

The development of global navigation satellite system (GNSS) data networks has offered an effective way to monitor the ionosphere continuously in the last two decades. Many two-dimensional ionospheric total electron content (TEC) models are constructed based on dual-frequency GNSS measurements, including the global ionospheric map (GIM) (e.g., Mannucci et al., 1998; Schaer, 1999). To generate the GIM, a mathematical model, such as spherical harmonic function is employed to express the global ionospheric TEC and the model parameters are estimated using GNSS measurements from global stations. Then the vertical TEC (VTEC) values on the global grids are computed using the ionospheric model parameters. In 1998, the international GNSS service (IGS) began routinely provided individual and combined GIM products from different analysis centers (see website https://igs.org/wg/ionosphere/). Since then, the GIM has been widely employed in ionospheric monitoring (Jhuang et al., 2018; Liu et al., 2016; Ren et al., 2021), GNSS positioning (Macalalad et al., 2016; Ning et al., 2019) and other related areas (Keshin, 2012; Tulasi Ram et al., 2016).

One important work that assesses the performance of GIM products needs to be done before using them. The direct VTEC by dual-frequency altimeters is commonly used to validate the accuracy of GIM products (Chen et al., 2016; Jee et al., 2010; Li et al., 2020). In addition, the difference of slant total electron content (dSTEC) along a continuous satellite–receiver arc using GNSS phase observations is also developed as a frequently-used assessment of ionospheric TEC models (Feltens et al., 2011; Hernández-Pajares et al., 2017; Orús et al., 2005). Hernández-Pajares et al. (2017) indicates the altimeter VTEC and GNSS dSTEC assessments show consistency.

According to the results in Hernández-Pajares et al. (2009), the IGS final GIM products have the accuracy of 2.0–8.0 TEC units.

The performance of GIM products is influenced by various factors, including data coverage, model strategy, and ionospheric variations. Chen et al. (2016) indicates the accuracy of GIMs in ocean areas improves significantly after integrating GNSS, satellite altimetry, radio occultation and DORIS data. Nie et al. (2019) shows the quality of real-time GIM products improves with higher degree and order of the spherical harmonic expansions. Liu et al. (2019) finds the performance of GIMs products during geomagnetic perturbed period is approximately 1.1–1.9 times worse than that during the geomagnetic quiet period. The ionosphere is a high dynamic and variable region. In addition to geomagnetic disturbances, low-latitude areas experience another common type of ionospheric variations known as equatorial plasma bubble (EPB). EPBs typically occur after sunset and can lead to a depletion of ionospheric TEC, resulting in significant TEC gradients (Kelley et al., 2011). Interestingly, research indicates that geomagnetic activity is unnecessary for EPB generation: the EPB can occur on both geomagnetic disturbed days and quiet days (Carter et al., 2014).

Currently, the error of GIM derived TEC (GIM-TEC) during EPB event is still not involved. To provide more reliable assessment of GIM products, in this study, we will investigate the EPB-induced GIM-TEC error using IGS final products during the high solar activity year of 2014.

2. Methodology

Here, the frequently-used GNSS dSTEC parameter is employed to assess the error of GIM-TEC during EPB event. Before establishing the dSTEC parameter, the observed and molded slant TEC (STEC) for a satellite–receiver pair should be computed firstly. In addition, the EPB events also need to be detected in advance. In this section, the methods for STEC calculation and EPB event detection are introduced firstly and then the method related to dSTEC assessments is presented.

2.1. Slant TEC Calculation and EPB Event Detection

For each satellite–receiver pair, the observed STEC (S_o) can be obtained using the geometry-free combination of dual-frequency GNSS carrier phase observations,

$$S_o(t) = \frac{1}{40.3}\frac{f_1^2 f_2^2}{f_1^2 - f_2^2}(L_1 - L_2 + \text{const} + \varepsilon) \tag{1}$$

where t is the epoch, f_1 and f_2 are the carrier phase frequencies, L_1 and L_2 are the carrier phase measurements, const is the unknown constant bias, including the carrier phase ambiguity and instrument bias, and ε is the noise. In addition, the so-called single-layer ionosphere assumption is employed to express the location, namely ionospheric pierce point (IPP), of the S_o (Schaer, 1999).

Then we use the S_o series to detect the EPB event. Here, the method developed by Tang et al. (2021) is employed to detect the EPB event. Figure 1 presents the schematic diagram for the EPB detection method. As shown in the figure, S_o (blue line) is the observed STEC series including an EPB event. Using the S_o series, the rate of TEC index (ROTI) is computed. The detailed computational processes of ROTI value are indicated in Pi et al. (1997). According to the ROTI series (black line), the EPB occurrence time period [T1, T2] is determined. Then we just fit the background STEC (S_b) during EPB event using a low-order polynomial while set the value of S_b outside the EPB event (before T1 and after T2) as the value of S_o. The green line is the whole S_b series. In this way, the difference between the S_o series and the S_b series for a satellite–receiver pair only lies in the period of EPB event.

Using the IGS GIMs, we can calculate the modeled STEC (S_m) for the satellite–receiver pair whose S_o include the EPB signal. The vertical TEC (V_m) at IPP of the satellite–receiver pair is first extracted from the IGS GIMs. Here, the linear interpolation strategy is employed. Specifically, the bivariate interpolation using the nearest four grid points in space and interpolation between consecutive rotated TEC maps in time are applied. The detailed computational processes are indicated in Schaer et al. (1998). Then we convert the V_m to the slant direction using a project factor

$$S_m(t) = M(e(t)) \cdot V_m(t) \tag{2}$$

where $M(e(t)) = 1/\sqrt{1 - \left(\frac{R}{R+H}\cos(e(t))\right)^2}$ is the project factor, R is the earth radius, H is the single-layer height, and e is the satellite elevation.

2.2. GNSS dSTEC Assessments

According to Hernández-Pajares et al. (2017), dSTEC is defined as the difference between the given STEC and the STEC at the highest satellite elevation for a satellite–receiver pair:

$$dS(t) = S(t) - S(e_{\max}) \tag{3}$$

where dS and S are dSTEC and STEC in TEC units (1 TECU = $10^{16}/\text{m}^2$), $e_{\max}$ is the highest satellite elevation.

Using Equation 3, we can obtain the observed dSTEC (dS_o), background dSTEC (dS_b) and modeled dSTEC (dS_m), respectively. Obviously, the unknown constant bias (const) in Equation 1 is eliminated when compute the observed dSTEC using Equation 3. Figure 2 presents the schematic diagram for these three series. Then, the differences ($dS_o - dS_m$) and ($dS_b - dS_m$) can present the final GIM-TEC errors (including EPB signal) and the GIM-TEC errors for absence of EPB, respectively.

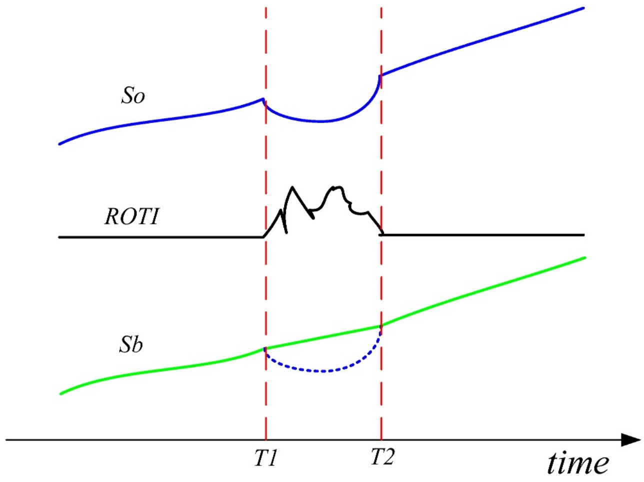

Figure 1. Schematic diagram for the equatorial plasma bubble (EPB) detection method. The blue line, black line and green line represent the S_o, rate of TEC index and S_b series, respectively. The red dotted lines indicate the EPB occurrence time period [T1, T2]. The blue dotted line is the part of S_o during EPB event for comparison.

To investigate the magnitude and percentage of EPB-induced GIM-TEC errors, for each satellite-receiver pair, we define two parameters as follow

$$\begin{cases} E_a = \dfrac{A_{P2} - A_{P1}}{N} = \dfrac{\sum|dS_o - dS_m| - \sum|dS_b - dS_m|}{N} \\ R_a = \dfrac{A_{P2} - A_{P1}}{A_{EPB}} = \dfrac{\sum|dS_o - dS_m| - \sum|dS_b - dS_m|}{\sum|dS_o - dS_b|} \end{cases} \tag{4}$$

where E_a is the average of EPB-induced GIM-TEC errors, R_a is the area ratio, N is the epoch numbers of an EPB event, A_{EPB} is the "area" of EPB, which is defined as the sum of TEC depletion multiply by time interval, A_{P1} and A_{P2} are the areas of P1 and P2 plotted in Figure 2. Here, we use the epoch number to represent the time interval. So the unit of area is also TECU. As shown in Figure 2, the "area" of the EPB is divided into two parts (P1 and P2) by the "line" of dS_m. Obviously, the area magnitudes of P1 and P2 can illustrate the difference between (dS_o-dS_m) and (dS_b-dS_m). According to the definition, the domain of R_a is $[-1, 1]$. If $R_a = 1$, the dS_m series is above the EPB and the GIM-TEC errors during the EPB event are all increased. Similarly, if $R_a = -1$, the dS_m series is below the EPB and the GIM-TEC errors are all reduced. For other values of R_a, the dS_m series is across the EPB and there are increased and reduced errors similarly. Particularly, the increased and reduced errors are same if $R_a = 0$ ($A_{P1} = A_{P2}$). Then, the E_a value is also equal to 0 TECU.

3. Results and Discussions

3.1. Data Description

As shown in Figure 3, 8 IGS GNSS stations distributed around geomagnetic equator during 2014 are employed to investigate the performance of the IGS GIM products. 2014 is a high solar activity year in which the EPB frequently occurred. The GNSS data with 30-s sampling and GIM products with 2.5° × 5° spatial resolution and 2-hr time resolution were collected from the Crustal Dynamics Data Information System (CDDIS) data center. In addition, the geomagnetically disturbed days in 2014 were excluded to avoid the effects of geomagnetic activities. The elevation mask angle was set as 30° for each satellite–receiver pair to reduce the errors in low angles. The height of single-layer is set to 350 km, which is a common value in previous studies.

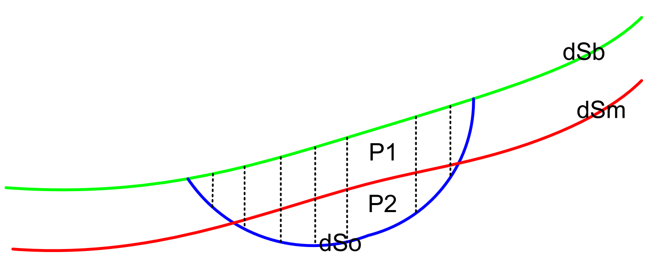

Figure 2. Diagram of the dS_o series (blue line), dS_b series (green line) and dS_m series (red line) for a satellite–receiver pair.

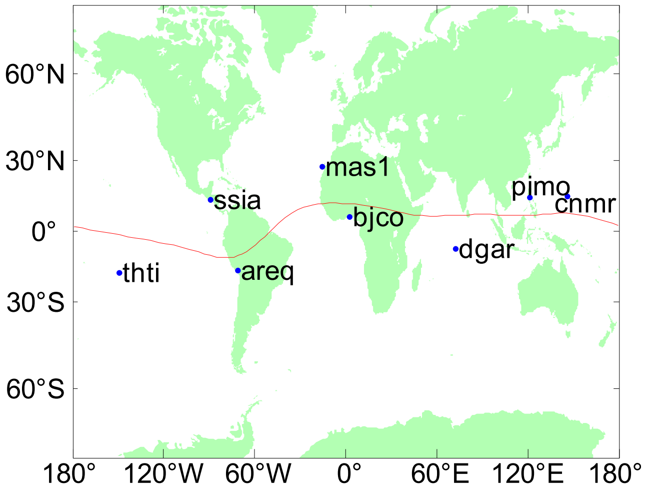

Figure 3. Distribution of global navigation satellite system stations (blue points). The red line represents the geomagnetic equator.

3.2. EPBs' Effect on dSTEC Assessment

Figure 4 presents a case of dSTEC series by station AREQ and satellite PRN 10 on day of year (DOY) 57, 2014. The blue line and green line in top panel indicate the S_o series and S_b series, respectively; correspondingly, the blue line and green line in bottom panel indicate the dS_o series and dS_b series, respectively. The red lines in top and bottom panels indicate the satellite elevation series. As shown in top panel, in this case, an EPB event occurs during 7:15–8:00 UT and is observed at the highest satellite elevation. The difference between S_o series and S_b series is only during the period of the EPB event. This is reasonable and due to the EPB detection method. However, as shown in bottom panel, not only the difference during the period of the EPB event, there is a bias (black double arrow) outside the period of the EPB event between dS_o series and dS_b series. In addition, similar biases are also observed by other satellite–receiver pairs with total number of 544, suggesting it is a common phenomenon.

The cause leading to this bias is due to the different STEC at the highest satellite elevation for S_o series and S_b series when computing the dSTEC values (see top panel in Figure 4). Obviously, this bias will also exist when computing the difference between dS_o series and dS_m series, leading to a fake bias in GIMs using the dSTEC assessment. The magnitude of the bias depends on the location of IPP with the highest satellite elevation in EPB structure. That is to say, if the IPP with the highest satellite elevation is located in the area with maximum TEC depletion, the bias is also maximized. Previous studies show the maximum TEC depletion can be up to dozens of TECUs (Portillo et al., 2008; Tang & Chen, 2022). So, the bias can also very large and not negligible. To eliminate the effect, the dS_o series that an EPB event is observed at the highest satellite elevation is needed to be excluded.

3.3. Error of GIM-TEC During EPB Event

After deleting the EPB events observed at the highest satellite elevation, there are total 591 dS_o series including EPB signals obtained by 8 selected stations during 2014. Figure 5 plots a case of various dSTEC series (top panel) and corresponding differences (bottom panel) by station CNMR and satellite PRN 20 on DOY 66, 2014. As shown in the figure, the values of $(dS_o - dS_m)$ and $(dS_b - dS_m)$ are same outside of the EPB event compared to the case in Figure 4. The absolute values of $(dS_o - dS_m)$ are larger than that of $(dS_b - dS_m)$ during the EPB event. Figure 6 plots a another case of various dSTEC series (top panel) and corresponding differences (bottom panel) by station CNMR and satellite PRN 1 on DOY 99, 2014. As shown in the figure, the absolute values of $(dS_o - dS_m)$ are smaller than that of $(dS_b - dS_m)$ during the EPB event. This suggests that the error of GIM-TEC can be both increased and reduced during the EPB event. The sign of EPB-induced GIM-TEC errors are mainly determined by the magnitude relationship between dS_b and dS_m (or S_b and S_m). If $dS_b < dS_m (S_b < S_m)$, EPB-induced GIM-TEC errors will increase and vice versa.

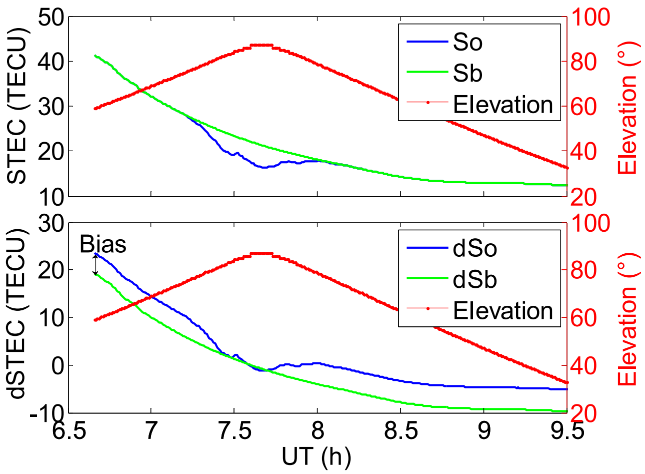

Figure 4. A case of difference of slant total electron content series that an equatorial plasma bubble event is observed at the highest satellite elevation by station AREQ and satellite PRN 10 on DOY 57, 2014.

The R_a values are computed for all the 591 satellite–receiver pairs during 2014 and the percentage distribution of R_a values is plotted in Figure 7 (left panel). As show in the figure, the maximum percentage is about 47% for $R_a = 1$, the second largest percentage is about 10% for $R_a = -1$ and the remaining R_a values are generally below 5%. In addition, the percentage for $R_a > 0$ ($R_a < 0$) is about 76% (24%). These results show nearly half of satellite–receiver pairs have totally increased GIM-TEC errors and about 10% satellite–receiver pairs have totally decreased GIM-TEC errors during the EPB event. To discuss the correlation between R_a and the magnitude of EPB, the R_a versus EPB area is also plotted in Figure 7 (right panel). Here, the EPB area could serve as a parameter to represent the magnitude of EPB. As shown in the figure, the correlation between R_a and EPB area is not significant: the correlation coefficient is only 0.046. For example, the value of R_a could be

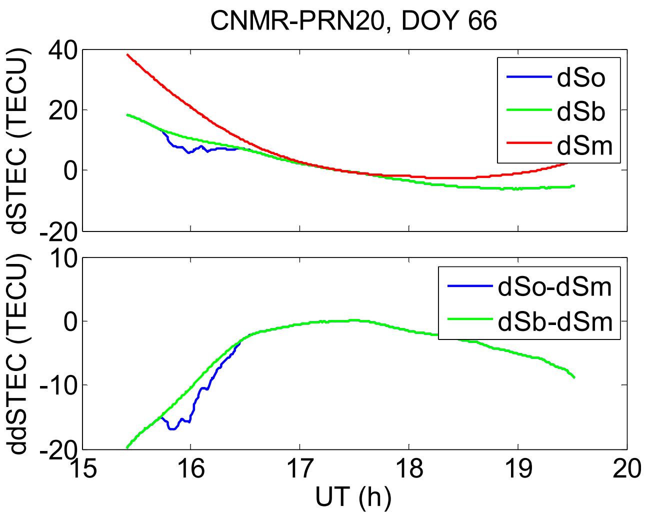

Figure 5. A case of various difference of slant total electron content series and corresponding differences by station CNMR and satellite PRN 20 on DOY 66, 2014. The blue line, green line and red line in top panel indicate the dS_o series, dS_b series and dS_m series, respectively. The blue line and green line in bottom panel indicate the $(dS_o - dS_m)$ series, and the $(dS_b - dS_m)$ series, respectively.

equal to 1 both for small and large EPB areas. This suggests increasing or decreasing the GIM-TEC errors is unrelated to the magnitude of EPB.

Similarly, the E_a values are also computed for all the 591 satellite–receiver pairs during 2014 and plotted in Figure 8. As shown in the figure, there are more frequent EPB events (dense blue circles) during spring and autumn equinoxes, which is consistent to the reported seasonal characteristics of EPB occurrence (Tsunoda, 1985). The E_a values are mainly at −5 to 5 TECU, and the maximum (minimum) is close to 10 TECU (−10 TECU). In addition, according to Figure 7 (left panel), obviously, the percentage of positive (negative) E_a is also 76% (24%).

Here, the EPB-induced GIM-TEC error is based on the dSTEC assessment, which is actually a value in slant direction. As we known, the error of GIM-TEC provided to users is a value in vertical direction. For a single epoch t during EPB event, according to Equation 4, the EPB-induced GIM-TEC error is

$$\Delta S_{\mathrm{EPB}}(t) = \begin{cases} dS_b(t) - dS_o(t), dS_m(t) \geq dS_b(t) \\ dS_o(t) - dS_b(t), dS_m(t) \leq dS_o(t) \\ dS_b(t) + dS_o(t) - 2dS_m(t), dS_o(t) < dS_m(t) < dS_o(t) \end{cases} \tag{5}$$

For $dS_m(t) \geq dS_b(t)$ or $dS_m(t) \leq dS_o(t)$,

$$\Delta S_{EPB}(t) = \pm(S_b(t) - S_o(t)) = \pm M(t) \cdot (V_b(t) - V_o(t)) \tag{6}$$

So, it can be directly converted to vertical direction with a mapping factor. For $dS_o(t) < dS_m(t) < dS_b(t)$,

$$\begin{aligned} \Delta S_{\mathrm{EPB}}(t) &= (S_b(t) + S_o(t) - 2S_m(t)) - 2(S_b(e_{\max}) - S_m(e_{\max})) \\ &= M(t) \cdot (V_b(t) + V_o(t) - 2V_m(t)) - 2M(e_{\max}) \cdot (V_b(e_{\max}) - V_m(e_{\max})) \end{aligned} \tag{7}$$

At this case, the converted error is existed due to $M(t) > M(e_{\max})$. However, above statistical results show most of $\Delta S_{\mathrm{EPB}}(t)$ meet Equation 6. In addition, for $dS_o(t) < dS_m(t) < dS_b(t)$, if $dS_m(t)$ is close to $dS_o(t)$ or $dS_b(t)$, $\Delta S_{EPB}(t)$ will approximately meets Equation 6; if $dS_m(t)$ is close to $(dS_o(t) + dS_b(t))/2$, its value will be small. So, we can generally convert $\Delta S_{EPB}(t)$ to the vertical direction with a mapping factor.

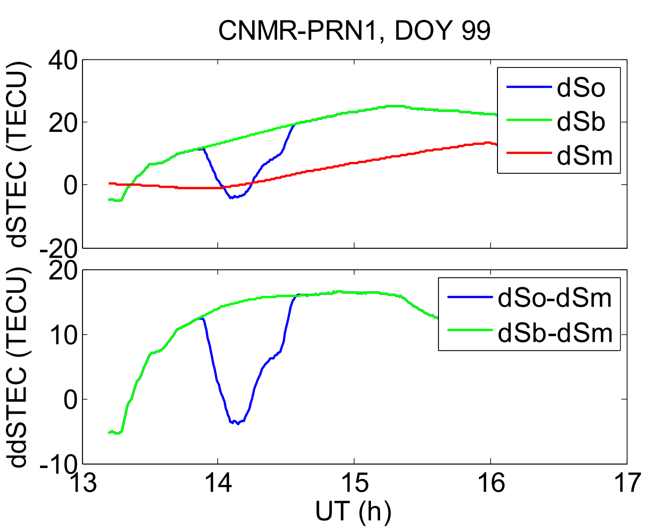

Figure 6. Same to Figure 5 but for a case of various difference of slant total electron content series and corresponding differences by station CNMR and satellite PRN 1 on DOY 99, 2014.

Above results show the absolute error of GIM-TEC can both increase and decrease during EPB event. As seen from Figures 4–6, the TEC gradients are very obvious in observed STEC or dSTEC series with an EPB signal. However, the curves of modeled dSTEC are very smooth during EPB event (see the top panels of Figures 5 and 6). Actually, similar results are observed for all the 591 satellite–receiver pairs. That is to say, the structure of EPB is unable to be captured by the GIM-TEC series. This can mainly attributed to the low spatial-temporal resolution of GIM products. Previous studies show the duration and zonal scale of EPB are generally smaller than 1 hr and 1.5°, respectively (Ji et al., 2013; Tang & Chen, 2022). In addition, the linear interpolation method to calculate the GIM-TEC is also difficult to catch the nonlinear profile of EPB.

Generally, the occurrences of EPB can reduce the performance of GIM products. First, most of EPBs can further add the absolute GIM-TEC errors. This will exert an adverse effect on space weather services which need absolute ionospheric corrections from GIM products. One common example is

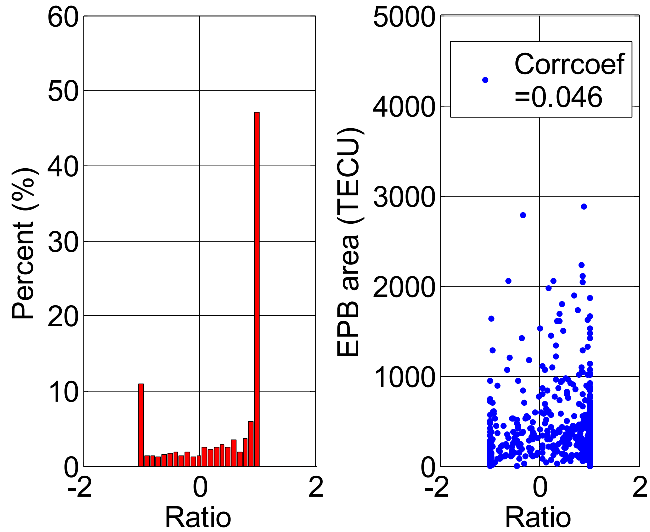

Figure 7. Percentage distribution of R_a values (left panel) and the relationship between R_a and equatorial plasma bubble area (right panel).

the GNSS single-frequency point positioning technique (Ning et al., 2019): the increased ionospheric correction errors will finally reduce the positioning accuracy. In addition, the occurrence of EPB can generate huge TEC gradients in ionosphere. However, the EPB-induced TEC gradients cannot be captured by the TEC series extracted from GIM. The TEC gradients are harmful to many applications relied on high-precision relative ionospheric corrections such as ground-based augmentation system for aviation safety (Affonso et al., 2022) and GNSS precise positing with ionospheric constraints (Zhang et al., 2013). So, the utilities of GIM-TEC will degrade under these circumstances.

4. Conclusions

We investigate the error of GIM-TEC during EPB event using GNSS stations distributed around the geomagnetic equator during the high solar activity year of 2014. The frequently-used dSTEC assessment method is checked firstly. We note that there is a fake bias in the observed dSTEC series when an EPB is observed at the highest satellite elevation. The observed results show the GIM-TEC error can increase or decrease when an EPB occurred. Then, the magnitude and percentage of extra GIM-TEC error induced by EPB are investigated. The

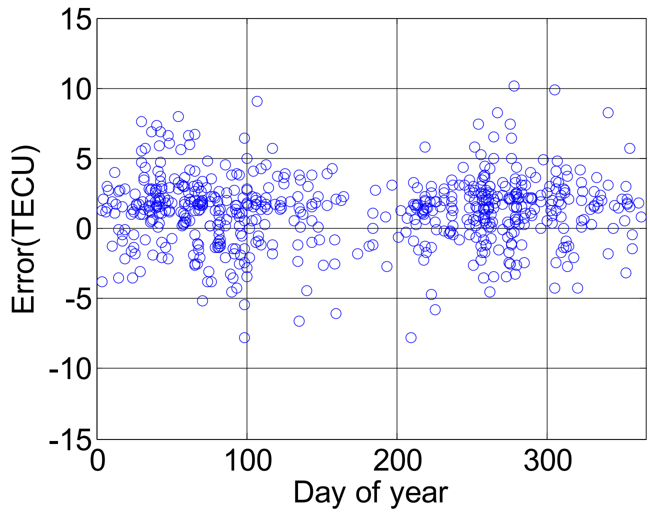

Figure 8. The average of EPB-induced GIM-TEC error during 2014.

results show that nearly half (about 10%) of satellite–receiver pairs have totally increased (decreased) GIM-TEC error during the period of EPB event, and the sign of EPB-induced error is not related to the EPB magnitude. As for the magnitude of average EPB-induced error, it is mainly at −5 to 5 TECU with 76% (24%) of positive (negative) values, and the maximum (minimum) is close to 10 TECU (−10 TECU). In addition, the structure of EPB is unable to be captured by the GIM-TEC series due to the low spatial-temporal resolution and linear interpolation method.

Data Availability Statement

Global navigation satellite system data and IGS-GIMs are available from the public website of CDDIS (https://cddis.nasa.gov/Data_and_Derived_Products/GNSS/GNSS_data_and_product_archive.html). Please select the data type on the left sidebar ("Daily 30-s data" for GNSS data and "Ionosphere/Troposphere" for IGS-GIMs). For a new user, sign-up is necessary at website https://urs.earthdata.nasa.gov/users/new. The geomagnetic activities data are publicly available from https://kp.gfz-potsdam.de/en/data.

Acknowledgments

The authors acknowledge the IGS for providing the GNSS data and GIMs products and GFZ for providing the geomagnetic activities data. This study was supported by the National Natural Science Foundation of China (Grant number 42274017), Guangdong Basic and Applied Basic Research Foundation (Grant number 2023A1515030184) and Hong Kong General Research Fund (Grant number 15230823).

References

Affonso, B. J., Moraes, A., Sousasantos, J., Marini-Pereira, L., & Pullen, S. (2022). Strong ionospheric spatial gradient events induced by signal propagation paths aligned with equatorial plasma bubbles. *IEEE Transactions on Aerospace and Electronic Systems*, *58*(4), 2868–2879. https://doi.org/10.1109/TAES.2022.3144622

Carter, B. A., Retterer, J. M., Yizengaw, E., Groves, K., Caton, R., McNamara, L., et al. (2014). Geomagnetic control of equatorial plasma bubble activity modeled by the TIEGCM with Kp. *Geophysical Research Letters*, *41*(15), 5331–5339. https://doi.org/10.1002/2014GL060953

Chen, P., Yao, Y., & Yao, W. (2016). Global ionosphere maps based on GNSS, satellite altimetry, radio occultation and DORIS. *GPS Solutions*, *21*(2), 639–650. https://doi.org/10.1007/s10291-016-0554-9

Feltens, J., Angling, M., Jackson-Booth, N., Jakowski, N., Hoque, M., Hernández-Pajares, M., et al. (2011). Comparative testing of four ionospheric models driven with GPS measurements. *Radio Science*, *46*(6), 1–11. https://doi.org/10.1029/2010RS004584

Hernández-Pajares, M., Juan, J. M., Sanz, J., Orus, R., Garcia-Rigo, A., Feltens, J., et al. (2009). The IGS VTEC maps: A reliable source of ionospheric information since 1998. *Journal of Geodesy*, *83*(3–4), 263–275. https://doi.org/10.1007/s00190-008-0266-1

Hernández-Pajares, M., Roma-Dollase, D., Krankowski, A., García-Rigo, A., & Orús-Pérez, R. (2017). Methodology and consistency of slant and vertical assessments for ionospheric electron content models. *Journal of Geodesy*, *91*(12), 1405–1414. https://doi.org/10.1007/s00190-017-1032-z

Jee, G., Lee, H. B., Kim, Y. H., Chung, J. K., & Cho, J. (2010). Assessment of GPS global ionosphere maps (GIM) by comparison between CODE GIM and TOPEX/Jason TEC data: Ionospheric perspective. *Journal of Geophysical Research*, *115*(A10). https://doi.org/10.1029/2010JA015432

Jhuang, H. K., Tsai, T. C., Lee, L. C., & Ho, Y. Y. (2018). Ionospheric tidal waves observed from global ionosphere maps: Analysis of total electron content. *Journal of Geophysical Research: Space Physics*, *123*(8), 6776–6797. https://doi.org/10.1029/2018JA025242

Ji, S., Chen, W., Wang, Z., Xu, Y., Weng, D., Wan, J., et al. (2013). A study of occurrence characteristics of plasma bubbles over Hong Kong area. *Advances in Space Research*, *52*(11), 1949–1958. https://doi.org/10.1016/j.asr.2013.08.026

Kelley, M. C., Makela, J. J., de La Beaujardière, O., & Retterer, J. (2011). Convective ionospheric storms: A review. *Reviews of Geophysics*, *49*(2). https://doi.org/10.1029/2010RG000340

Keshin, M. (2012). A new algorithm for single receiver DCB estimation using IGS TEC maps. *GPS Solutions*, *16*(3), 283–292. https://doi.org/10.1007/s10291-011-0230-z

Li, Z., Wang, N., Hernández-Pajares, M., Yuan, Y., Krankowski, A., Liu, A., et al. (2020). IGS real-time service for global ionospheric total electron content modeling. *Journal of Geodesy*, *94*(3), 32. https://doi.org/10.1007/s00190-020-01360-0

Liu, A., Wang, N., Li, Z., Wang, Z., & Yuan, H. (2019). Assessment of NeQuick and IRI-2016 models during different geomagnetic activities in global scale: Comparison with GPS-TEC, dSTEC, Jason-TEC and GIM. *Advances in Space Research*, *63*(12), 3978–3992. https://doi.org/10.1016/j.asr.2019.02.032

Liu, J., Hernandez-Pajares, M., Liang, X., An, J., Wang, H., Chen, R., et al. (2016). Temporal and spatial variations of global ionospheric total electron content under various solar conditions. *Journal of Geodesy*, *91*(5), 485–502. https://doi.org/10.1007/s00190-016-0977-7

Macalalad, E. P., Tsai, L. C., & Wu, J. (2016). Performance evaluation of different ionospheric models in single-frequency code-based differential GPS positioning. *GPS Solutions*, *20*(2), 173–185. https://doi.org/10.1007/s10291-014-0422-4

Mannucci, A. J., Wilson, B. D., Yuan, D. N., Ho, C. H., Lindqwister, U. J., & Runge, T. F. (1998). A global mapping technique for GPS-derived ionospheric total electron content measurements. *Radio Science*, *33*(3), 565–582. https://doi.org/10.1029/97RS02707

Nie, Z., Yang, H., Zhou, P., Gao, Y., & Wang, Z. (2019). Quality assessment of CNES real-time ionospheric products. *GPS Solutions*, *23*(1), 11. https://doi.org/10.1007/s10291-018-0802-2

Ning, Y., Han, H., & Zhang, L. (2019). Single-frequency precise point positioning enhanced with multi-GNSS observations and global ionosphere maps. *Measurement Science and Technology*, *30*(1), 015013. https://doi.org/10.1088/1361-6501/aaf0f6

Orús, R., Hernández-Pajares, M., Juan, J. M., & Sanz, J. (2005). Improvement of global ionospheric VTEC maps by using kriging interpolation technique. *Journal of Atmospheric and Solar-Terrestrial Physics*, *67*(16), 1598–1609. https://doi.org/10.1016/j.jastp.2005.07.017

Pi, X., Mannucci, A. J., Lindqwister, U. J., & Ho, C. M. (1997). Monitoring of global ionospheric irregularities using the worldwide GPS network. *Geophysical Research Letters*, *24*(18), 2283–2286. https://doi.org/10.1029/97GL02273

Portillo, A., Herraiz, M., Radicella, S. M., & Ciraolo, L. (2008). Equatorial plasma bubbles studied using African slant total electron content observations. *Journal of Atmospheric and Solar-Terrestrial Physics*, *70*(6), 907–917. https://doi.org/10.1016/j.jastp.2007.05.019

Ren, X., Zhang, J., Chen, J., & Zhang, X. (2021). Global ionospheric modeling using multi-GNSS and upcoming LEO constellations: Two methods and comparison. *IEEE Transactions on Geoscience and Remote Sensing*, *60*, 1–15. https://doi.org/10.1109/TGRS.2021.3050413

Schaer, S. (1999). *Mapping and predicting the Earth's ionosphere using the global positioning system* (Vol. 59). Zürich, Switzerland: Institut für Geodäsie und Photogrammetrie, Eidg. Technische Hochschule Zürich.

Schaer, S., Gurtner, W., & Feltens, J. (1998). IONEX: The ionosphere map exchange format version 1. In *Proceedings of the IGS AC workshop, IGS technical note, Darmstadt, Germany* (Vol. 9).11.

Tang, L., & Chen, G. (2022). Equatorial plasma bubble detection using vertical TEC from altimetry satellite. *Space Weather*, *20*(8), e2022SW003142. https://doi.org/10.1029/2022SW003142

Tang, L., Louis, O. P., Chen, W., & Chen, M. (2021). A ROTI-aided equatorial plasma bubbles detection method. *Remote Sensing*, *13*(21), 4356. https://doi.org/10.3390/rs13214356

Tsunoda, R. T. (1985). Control of the seasonal and longitudinal occurrence of equatorial scintillations by the longitudinal gradient in integrated E region Pedersen conductivity. *Journal of Geophysical Research*, *90*(A1), 447–456. https://doi.org/10.1029/JA090iA01p00447

Tulasi Ram, S., Su, S., Tsai, L. C., & Liu, C. H. (2016). A self-contained GIM-aided Abel retrieval method to improve GNSS-Radio Occultation retrieved electron density profiles. *GPS Solutions*, *20*(4), 825–836. https://doi.org/10.1007/s10291-015-0491-z

Zhang, H., Gao, Z., Ge, M., Niu, X., Huang, L., Tu, R., & Li, X. (2013). On the convergence of ionospheric constrained precise point positioning (IC-PPP) based on undifferential uncombined raw GNSS observations. *Sensors*, *13*(11), 15708–15725. https://doi.org/10.3390/s131115708